




Detection of a Cobalt-Containing Interphase at the $\text{Li}_6\text{PS}_5\text{Cl-NMC111}$ Interface by In Situ μXANES and EIS

Alyssa M. Stavola,¹ Eric K. Zimmerer,¹ Xiao Sun,² Kamila C. Wawer,¹ Andrew M. Kiss,³ Tongtai Ji,^{2,*} Hongli Zhu,^{2,z} and Joshua W. Gallaway^{1,**,z} 

¹Department of Chemical Engineering, Northeastern University, Boston, Massachusetts 02115, United States of America

²Department of Mechanical and Industrial Engineering, Northeastern University, Boston, Massachusetts 02115, United States of America

³National Synchrotron Light Source II, Brookhaven National Laboratory, Upton, New York 11973, United States of America

Sulfide electrolyte all-solid-state lithium batteries (ASLBs) with uncoated $\text{Li-Ni}_x\text{Mn}_y\text{Co}_{1-x-y}\text{O}_2$ (NMC) cathodes suffer from a large capacity loss during initial cycling and an increase in cell impedance. Decomposition reactions are known to occur at the $\text{Li}_6\text{PS}_5\text{Cl-NMC111}$ interface due to incompatibility between the two materials. If a stabilizing coating is applied to the NMC, it delivers full capacity during initial charge. However, the loss in capacity during discharge still occurs. The interface was studied by μXANES and through EIS analysis. A chemically-formed interphase was detected by μXANES , evident from reduction of Co at an uncoated NMC particle surface. This interphase was produced by decomposition at rest. To study the effect of the interphase on electrochemically active surface area, piecewise in situ EIS was performed and the data was modeled using a transmission line model (TLM). The charge transfer resistance R_{CT} was used to estimate the volume specific active surface area (a_{act}). The median value for a_{act} was 296 cm^{-1} , a factor of 7.5 lower than the theoretical value of 2216 cm^{-1} . This provided evidence of a lower electrochemically active surface area in the ASLB.

© 2024 The Author(s). Published on behalf of The Electrochemical Society by IOP Publishing Limited. This is an open access article distributed under the terms of the Creative Commons Attribution 4.0 License (CC BY, <http://creativecommons.org/licenses/by/4.0/>), which permits unrestricted reuse of the work in any medium, provided the original work is properly cited. [DOI: 10.1149/1945-7111/ad29c6]



Manuscript submitted December 11, 2023; revised manuscript received January 24, 2024. Published March 4, 2024.

All-solid-state lithium batteries (ASLBs) with sulfide based electrolytes are considered promising because the high conductivity of argyrodite-type sulfides could enable practical devices.¹⁻⁴ However, when using with $\text{Li-Ni}_x\text{Mn}_y\text{Co}_{1-x-y}\text{O}_2$ (NMC) cathodes, these ASLBs show capacity loss in the first cycle. This has several contributing causes, such as formation of a chemical interphase, formation of an interphase during electrochemical cycling, and physical disconnection of the NMC and solid electrolyte. All these result in increased internal resistance at the interface, reducing the specific capacity.⁵ Understanding the nature of the reactions at the interface are important to developing practical sulfide-electrolyte ASLBs.

It is known that sulfide argyrodite solid-state electrolyte (SSE) $\text{Li}_6\text{PS}_5\text{Cl}$ decomposes where it contacts the NMC cathode particles, causing ionically insulating interphases to form and hindering the transport of lithium ions.⁶⁻⁹ The reactivity of layered oxide cathode materials and the SSE has prevented this battery from achieving high energy density and high cycle life.^{5,6} Forming a favorable and stable interphase is thought to be crucial to the success and implementation of high capacity ASLBs. This is analogous to the critical nature of the SEI in Li-ion batteries.

Past work has examined the NMC-argyrodite interface using XPS and SIMS, finding chemical decomposition produces sulfides while electrochemical cycling promotes sulfur oxides and phosphates.^{9,10} Separately, first-principles calculations determined likely high voltage decomposition products from the electrolyte itself include P_2S_5 , S, and PCl_3 without NMC reactions.¹¹ In situ EIS enables tracking time-dependent impedance evolutions, combined with modeling approaches like transmission line models (TLMs) to isolate individual resistances.^{12,13} Specifically, EIS analysis has shown passivation layers causing irreversible capacity losses, evolving tortuosity limiting conduction, and detectable impedance from the Li-depleted interfacial layer.^{5,14-16} Together, this *operando* perspective demonstrates a complex mechanistic interplay between chemical decomposition pathways consuming cathode and electrolyte species, along with passivation effects at a critical solid-solid

interface, fundamentally affects all-solid-state battery performance on the cathode side.

We have previously reported an *operando* analysis of Li^+ and e^- conduction across a composite cathode based on $\text{Li-Ni}_{1/3}\text{Mn}_{1/3}\text{Co}_{1/3}\text{O}_2$ (NMC111) and $\text{Li}_6\text{PS}_5\text{Cl}$ (LPSC) during initial cycling.¹⁷ This analysis indicated that conduction during initial cycling was subject to high tortuosity factors (τ^2) for both the LPSC and NMC phases. Because cathode performance was limited by conduction, we were unable to infer information about kinetic phenomena or the active surface area between the NMC and LPSC. Results for cells with coated and uncoated NMC were virtually identical.

Previous reports on chemical decomposition products in NMC-containing cathodes have shown evidence of sulfides. To our knowledge, direct evidence of redox state changes by the NMC transition metals has not been previously demonstrated. In the current work, micron-scale X-ray absorption near edge structure (μXANES) was used to scan microscopically across the LPSC-NMC interface. We directly observe the reduction of Co at the NMC surface, providing evidence of cobalt sulfides such as CoS and Co_3S_4 . A similar study was recently reported using Fe K-edge nXANES at the surface of LiFePO_4 in contact with a sulfide.¹⁸

We also performed in situ piecewise EIS on $(\text{Li/InLi})_6\text{PS}_5\text{Cl/NMC111/Li}_6\text{PS}_5\text{Cl}$ cells with 10 mg composite cathodes to study the evolution of impedances during cycling. This piecewise EIS allowed an estimation of the active surface area in a cell with uncoated NMC, which was $7.5\times$ lower than the theoretical value.

Experimental

Materials and synthesis.—The cathode active material (CAM) was $\text{Li-Ni}_{1/3}\text{Mn}_{1/3}\text{Co}_{1/3}\text{O}_2$ (NMC111). The SSE precursors P_2S_5 (99%), Li_2S (99.98%), and LiCl (99%) were purchased from Sigma-Aldrich. Argyrodite $\text{Li}_6\text{PS}_5\text{Cl}$ was synthesized by mechanical ball milling and then annealing treatment.¹⁹ A stoichiometric mixture of P_2S_5 , Li_2S , and LiCl was milled in a stainless steel jar (50 ml) with zirconia balls for 10 h at 500 rpm. The as-mixed precursors were sealed in a glass tube and annealed in a quartz tube furnace at $550\text{ }^\circ\text{C}$ for 6 h. The CAM coating of a 15–20 nm layer of $\text{Li}_{0.35}\text{La}_{0.5}\text{Sr}_{0.05}\text{TiO}_3$ (LLSTO) was performed as reported previously.⁶ Coated CAM is referred to in this work as NMC-LLSTO.

*Electrochemical Society Student Member.

**Electrochemical Society Member.

^zE-mail: j.gallaway@northeastern.edu; h.zhu@northeastern.edu

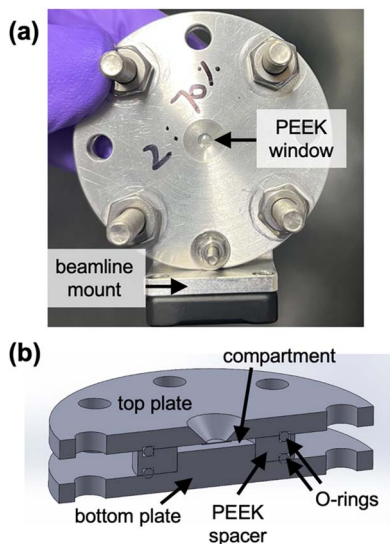


Figure 1. (a) The windowed in situ cell used for μ XANES experiments. The PEEK window where data was obtained is indicated. (b) Cut-away view showing the cell design.

Fabrication and cycling of ASLBs.—The CAM was mixed with LPSC in a 70/30 mass ratio to form the composite cathode powder. A 200 mg pellet of pure LPSC was pressed at 300 MPa to form the solid-state electrolyte separator. Composite cathode powder was cast onto the pellet at 100 MPa to form the composite cathode. A piece of In-Li was pressed to the other side of the separator pellet at 100 MPa to form the anode. Al and Cu foils were used for the cathode and anode current collectors. Cell cycling was performed under 50 MPa. Mass loading was 7.9 mg cm^{-2} in the cells in Fig. 2 and 5.6 mg cm^{-2} for the cells in Figs. 7–9. Cycling was accomplished using a constant current-constant voltage (CCCV) profile during the charge. The voltage limits were 2.5 and 4.0 vs In-Li (2.8 V–4.3 V vs Li/Li⁺).

Fabrication of liquid electrolyte cells.—Coin cells with liquid electrolytes were fabricated for comparison. The loading was matched to that of the full ASLB (5.6 mg cm^{-2}), and the same active material was used. The cathode consisted of 96% NMC111, 2% Super C65, and 2% PVDF. NMP was used to create a slurry with 61% solids. The slurry was cast on aluminum foil with a 50 μm drawdown cylinder. The cathodes were pressed and

punched with a 12.6 mm diameter and heated for 12 h under vacuum before being transferred to an argon atmosphere glovebox. CR2032 cells were assembled with two layers of Celgard 2320 and 1 M LiPF₆ in EC+EMC (3:7 in volume) with VC additive (MTI Corporation). The Li metal anode had a diameter of 5/8" and thickness of 0.75 mm.

In situ XRF mapping and μ XANES.—An in situ cell was designed, shown in Fig. 1. For the *in situ* spectroscopy, CAM was mixed with LPSC in two different mass ratios to form the composite cathode powder: 70/30 (70% CAM) and 10/90 (10% CAM). Cells were constructed with an X-ray transparent 2 mil polyether ether ketone (PEEK) window. Compression was calculated to be 50 MPa.

X-ray fluorescence mapping (XRF) was performed at 5-ID beamline (SRX) at NSLS-II.²⁰ XRF was completed for a $90 \mu\text{m} \times 90 \mu\text{m}$ region within these composite cathodes. Data were fit using the open-source software PyXRF.²¹ The beam size was approximately $900 \times 600 \text{ nm}$. For simplicity we assumed a pixel size of $1 \mu\text{m}^2$ for mapping experiments. μ XANES data were collected by varying incident energy across the Co and Ni K-edges at 7.7 and 8.3 keV, respectively. Incident energy was varied from 50 eV below the edge energy to 170 eV above to allow for normalization in Athena.²² When scanning incident energy, a smaller step size of 0.5 eV was used for greater resolution in the region from 10 eV below to 50 eV above the K-edge energy of the element in its metallic state. A step size of 4 eV was used outside of this region. For all incident energy values, a collection time of 1 second was used. Data were rebinned and edge-energies of Co and Ni standards were calibrated to their known values using Athena. Attenuation length for NMC was calculated to be 6–7.5 μm depending on which K-edge was being scanned. The length for LPSC was much longer, and thus incident X-rays penetrated the electrode until they encountered a particle of active material.

Piecewise in situ EIS.—Piecewise EIS was performed on NMC cathodes. A BioLogic SP-150 potentiostat was used within a frequency range of 1 MHz to 0.01 Hz, applying an excitation voltage amplitude of 10 mV, and recording 6 points per decade. Collection of the piecewise EIS was at a nominal rate of C/10, broken into 1 h increments. After a one hour rest, EIS was taken. For the transition line model (TLM) fitting the SSE separator layer (200 mg of LPSC) was calculated to amount to a 978 μm thick layer and this was corroborated with EDXRD imaging of full cells. This corresponded to a 41.28 Ω resistance of the separator SSE layer, and R_{SSE} was fixed to this value.

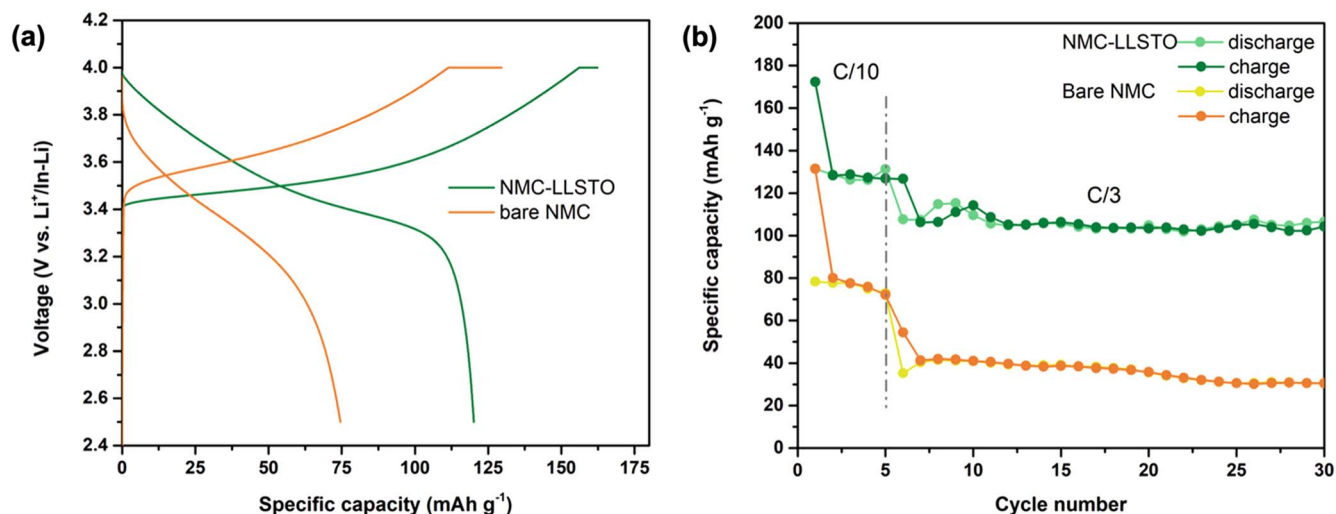


Figure 2. Electrochemical performance of cathodes prepared with bare NMC111 and NMC111 with a protective coating of LLSTO. (a) Voltage profiles of initial charge and discharge. (b) Specific capacities for 30 cycles. The bare NMC111 showed a significant capacity loss during the first charge, caused by chemical decomposition.

Results

Electrochemical cycling.—Cycling of ASLBs is shown in Fig. 2, comparing cells prepared with bare NMC and coated NMC-LLSTO. The cells began with a charge step, followed by discharge, with voltage curves shown in Fig. 2a. Five cycles were performed at C/10, with later cycles at C/3. The specific capacities are shown in Fig. 2b.

With a cathode interfacial coating, the full NMC capacity was accessed during the first charge (172 mAh g^{-1}). During the first discharge, there was a loss in capacity caused by irreversible reactions (121 mAh g^{-1}). With uncoated NMC, the first charge resulted in significantly lower capacity (132 mAh g^{-1}) than theoretically available in the NMC ($\sim 160 \text{ mAh g}^{-1}$). After the first discharge, capacity was even lower (76 mAh g^{-1}).

A loss in capacity can be caused by (i) conversion of active material to an electrochemically irreversible phase, or (ii) introduction of an internal resistance large enough to push the electrochemical activity of active material into a potential range outside of the battery operational window. An example of the latter case is formation of a resistive blocking layer that isolates available active material from the rest of the cell, rendering it unavailable.

It was clear from the above cycling results that the uncoated NMC suffered from a capacity loss on first charge that was not seen with a cathode coating. This loss during the first charge could be due to electrochemical events that happen under applied current, or chemical events that occur at rest, before cycling begins. Previous reports have shown evidence of S and P containing breakdown products.¹⁰ However, to our knowledge evidence of alteration of the NMC has been less discussed. If species originating in the NMC are converted to other materials, this would mean capacity loss mechanism (i) occurs to some extent, and the capacity losses are not only due to resistive layers adding overpotentials to the cell voltage.

In situ μ XANES of the $\text{Li}_6\text{PS}_5\text{Cl-NMC111}$ interface.—

Presumably, redox reactions occur at the interface where LPSC is in contact with the cathode active material. If LPSC is oxidized, the reduced compounds originate in the NMC. To specifically probe the LPSC-NMC interface, we employed a spatially resolved X-ray spectroscopic technique. The NMC particles (Fig. 3a) were roughly spherical with an average diameter of $9.3 \mu\text{m}$. However, there was distribution of particle sizes, with examples in Fig. 3b ranging across a factor of 7, from $2.9 \mu\text{m}$ to $20.5 \mu\text{m}$.

XRF mapping allowed composite materials to be imaged. Figure 4a shows a composite cathode with 10% NMC by mass and Fig. 4b shows a composite cathode with 70% NMC by mass. Areas with a low Co signal were occupied by either LPSC or void. The 70% composition was the optimal for battery performance, for example in the data shown in Fig. 2. Given the high-flux onto the sample and the high fluorescence yield from the particles, the 70%

CAM sample was difficult to analyze and find isolated particles for measurements.

To resolve isolated NMC particles, a 10% CAM case provided ample distance between particles. The brightness of the NMC particles indicated their relative proximity to the PEEK window. This means the particle at coordinates (65,65) in Fig. 4a was closest to the PEEK window.

Figure 5 shows the 10% NMC composite cathode with the individual elemental XRF mapping of Ni, Mn, Co, and S. The collocation of Ni, Mn, and Co marked the NMC particles. The S signal was anti-correlated to these, as S was found in the LPSC and was present in the regions left vacant by NMC. Fluorescence response was in proportion to element Z values: $\text{Ni} > \text{Co} > \text{Mn} \gg \text{S}$. From this series of scans, a particle of interest was chosen, marked in each panel by a white dashed box. This particle had other NMC particles in its “west” and “southwest” directions. However, to the north and east, only LPSC was in its vicinity.

This particle of interest was analyzed using μ XANES collected across the NMC particle interface. Figure 6a shows a detail of the XRF map with 21 μ XANES positions indicated by gray dots placed in the middles of the pixels. By collecting μ XANES at a grid of positions which spanned the particle interface we scanned for changes between the particle bulk and the interphase region formed at the interface where LPSC and uncoated NMC were in contact. Two such scans were performed in the “north” direction and one in the “east” direction. These were assigned a position value based on radius (P1-P8).

In Fig. 6 panels (b-e) these positions are given different colors. The XRF map in Fig. 6a was taken with the Si filter removed, causing a “halo” effect due to signal saturation in the bulk of the particle. At positions beyond those marked by dots in Fig. 6a, the Co and Ni K-edge μ XANES signals vanished, meaning these positions were beyond the particle interface. The Mn K-edge μ XANES data had a higher signal-to-noise ratio than that of Co and Ni, and consequently small variations in the μ XANES could not be observed with confidence.

μ XANES scans were used to examine the change in composition in the interphase region in contact with LPSC, as compared to the NMC bulk. The interface of the LPSC and NMC was measured at every position because these particles were in a 3-dimensional composite cathode. However, the interphase signal was drowned out by the bulk particle data at the positions closer to the center of the particle. The normalized absorption coefficients at each position are plotted for the K-edges of Co (Fig. 6b) and Ni (Fig. 6d). Black traces were the center of the particle and light blue was the location furthest from the center of the particle, which was largely composed of interphase.

Co metal has a K-edge of 7708.9 eV . In Fig. 6b the absorption edges were higher, indicating Co was in a more oxidized state. In NMC111 Ni, Mn, and Co have the nominal oxidation states of $2+$, $4+$, and $3+$.²³ In Ni-rich NMCs some of the Ni is oxidized to

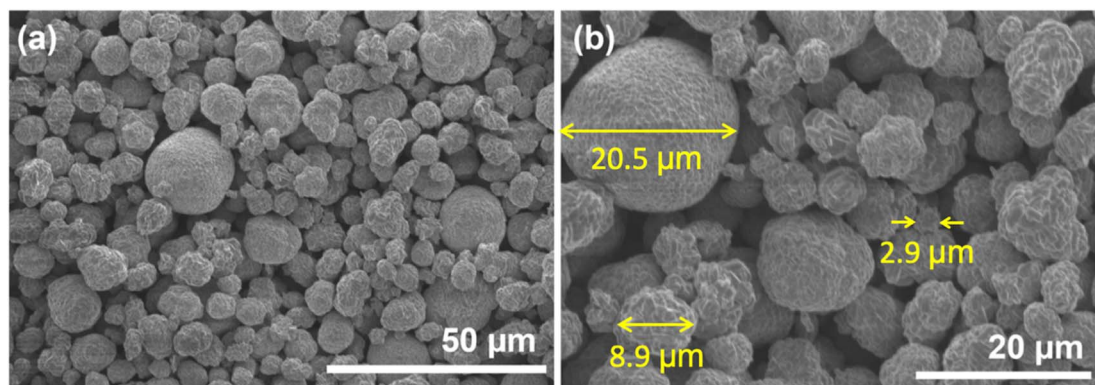


Figure 3. (a) SEM of the NMC111 particles. (b) Detail showing the range of particle sizes, which varied around the average of $9.3 \mu\text{m}$.

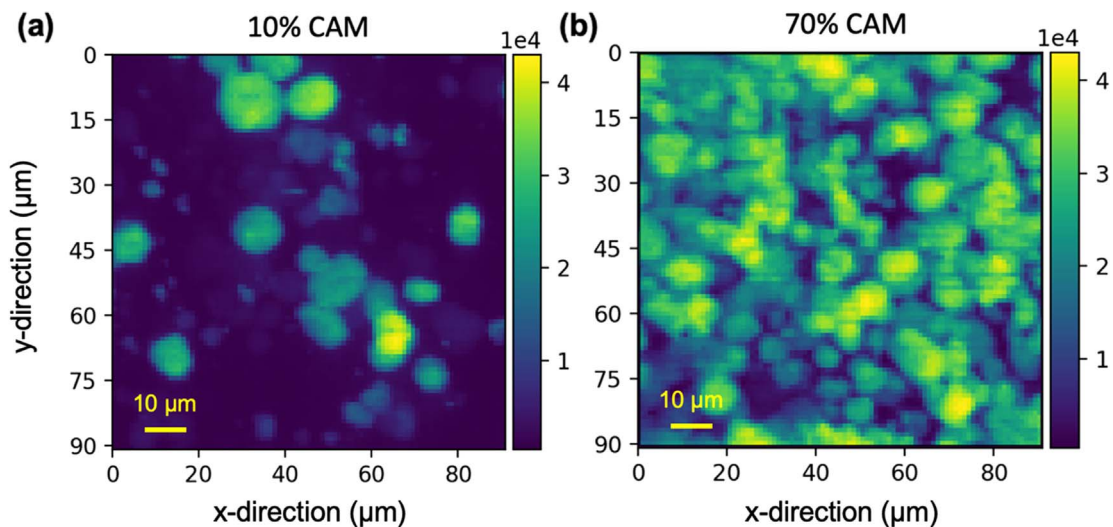


Figure 4. X-ray Fluorescence (XRF) mapping of Co used to demonstrate relative concentrations of NMC particles within composite cathodes with (a) 10% NMC by mass and (b) 70% NMC by mass.

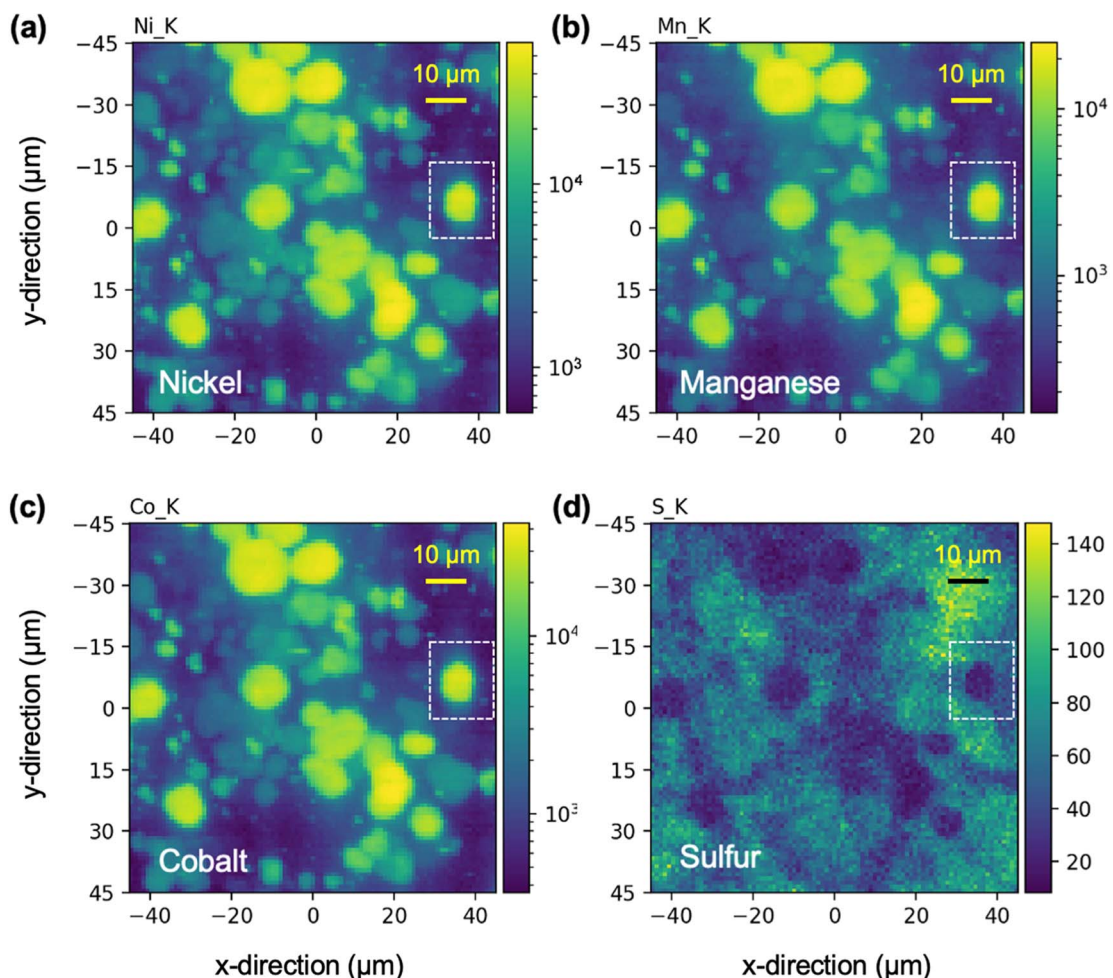


Figure 5. XRF mapping of a 90 μm × 90 μm region in a 10% NMC composite cathode. Fluorescence signals of (a) Ni, (b) Mn, and (c) Co overlap and allow for visualization of NMC particles. Fluorescence signal of (d) S is flipped, showing the exclusion of LPSC electrolyte by NMC particles.

maintain electroneutrality. Surface analyses of uncycled NMCs have been reported with a Co oxidation state of 3+ and also a mixture of 3+/4+.^{24–26}

In the derivative plot of the Co μ XANES (Fig. 6c) the edge energy is indicated by the large peak before the zero-crossing point,

which occurs at 7727.2 eV. Reports of Co XANES in the literature indicate that a shift to lower photon energy by about 4 eV is expected when comparing a Co²⁺ compound to an analogous Co³⁺ compound.^{27,28} In the positions closer to the interface of the particle (P7, P8) a smaller peak was observed at 7722.7 eV (marked by an

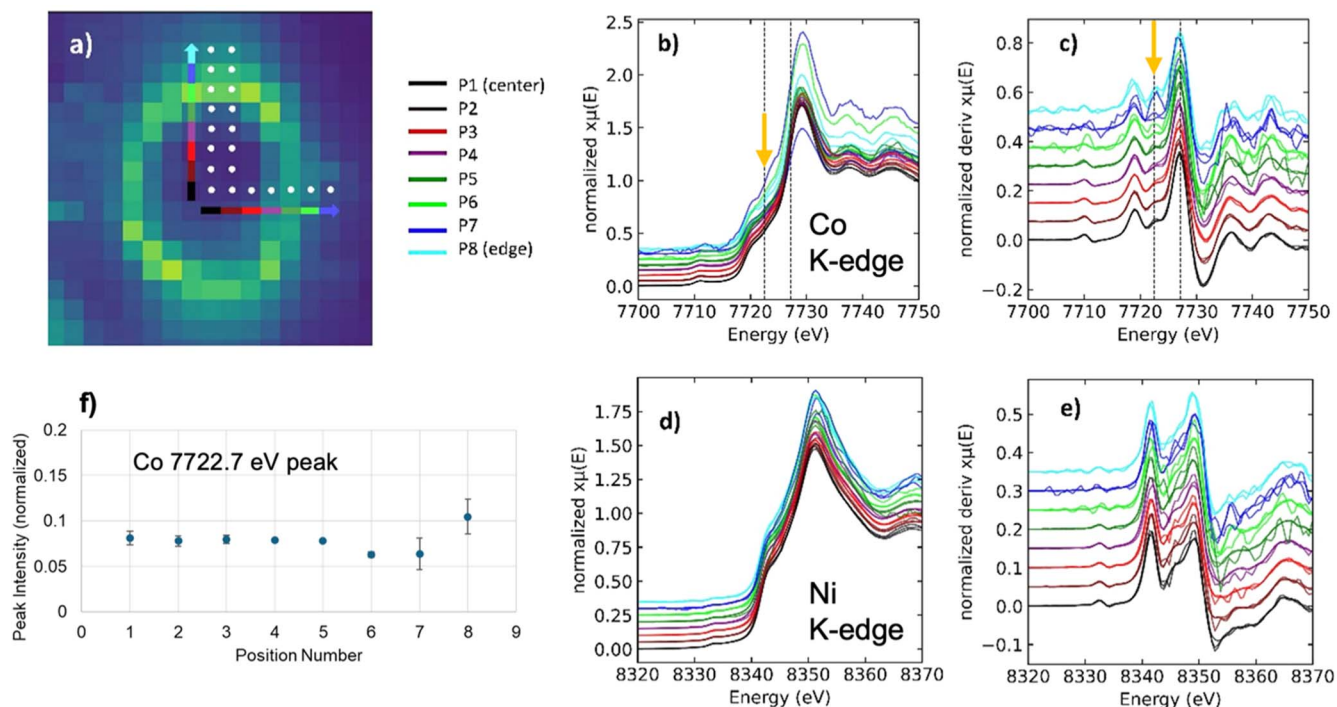


Figure 6. μ XANES analysis of the NMC particle of interest. (a) XRF map of the particle with the μ XANES positions marked. (b) For Co: the normalized absorption coefficients at each position. (c) For Co: the derivatives of the normalized absorption coefficients. (d), (e) The corresponding data for Ni. In panels (b)–(e) there is an arbitrary offset on the y-axis for clarity. (f) Values of the Co 7722.7 eV peak showing the interphase position 8 had a significantly higher intensity, indicating Co²⁺.

orange arrow), indicating the formation of a Co²⁺ species. Spatially-resolved intensity of the 7722.7 eV peak is shown in Fig. 6f, demonstrating a significant increase at the particle interface. The continued existence of the original peak at a higher energy indicated that some amount of Co³⁺ remained and was expected as XANES is an additive technique. For Ni there was no change in oxidation state between the interphase and bulk (Fig. 6e).

The reduction of Co suggests that NMC undergoes a redox reaction with LPSC electrolyte, as oxidation to Co⁴⁺ would be expected upon self-discharge. No change was observed in the oxidation state of Ni (Fig. 6e). The decoupling of Co and Ni oxidation states further indicates the breakdown of the NMC material at the interface. The presence of Co²⁺ suggested the formation of a cobalt sulfide such as CoS or Co₃S₄.

Jung et al. have previously reported XPS and SIMS analyses of both aged and cycled pellet cathodes.¹⁰ In aged cathodes that were not cycled, they found evidence of decomposition to sulfides, raising the possibility of NiS, CoS, MnS, or Li₂S if the components of the NMC participated in sulfide formation. They also found evidence of NiS in the XPS spectra.²⁹ However, involvement of the other metals was not specifically indicated. By using a microscopic technique to probe redox states at the LPSC-NMC interface, the results above demonstrated a measurable reduction of Co³⁺ to Co²⁺ at the NMC surface. This verified that Co participates in a redox reaction during chemical degradation. With an uncoated NMC, this confirms that active material was converted to other species, and that capacity loss was at least partially caused by active material loss.

Piecewise in situ EIS during cycling.—The evolution of electrochemical kinetics was studied by EIS. The piecewise EIS for cell charging shown in Fig. 7c (coated ASLB), Fig. 8a (uncoated ASLB), and Fig. 8b (liquid-electrolyte cell) were performed in the manner of a GITT-type experiment, with a galvanostatic period followed by a rest. The GITT cutoff voltage was 4 V, although there was relaxation during the rest after this. On the EIS plots, voltage after relation was the value reported.

Figures 7a–7b shows the piecewise cycling data of a full cell made with coated NMC-LLSTO. The cell underwent 8 charge steps at C/10 before the upper voltage limit was reached, followed by six discharge steps. Piecewise Nyquist plots for the charge are shown in Fig. 7c. For all piecewise steps the Nyquist plots had the appearance of a single semicircle with a low frequency tail characteristic of mass transport. At 1 MHz there was a high frequency resistance (HFR) of 38 Ω , which was mostly invariant during cycling.

The transition from semicircle to tail was at about 1 Hz, so the real impedance value (Z) at 1 Hz could be used as a characteristic impedance for the limiting process at each stage after the HFR was subtracted, essentially the width of the Nyquist plot semicircle. After the first hour of charge the characteristic impedance was 562 Ω . This value decreased with each step until 3.68 V when it was 214 Ω . Charge steps 7 and 8 showed an increase to a final value of 286 Ω . During discharge (Fig. 7d) the impedance increased to 938 Ω . The increase was particularly steep below 3.44 V. Evolution of the Nyquist plots did not follow a reversible path during the first charge-discharge cycle. This was expected because the cycling data showed a large capacity loss between the first charge and first discharge. The impedance increase began in the final steps of charge and continued through discharge. This indicated the processes causing capacity loss occurred during this period, and primarily at low voltages at the end of discharge, when the biggest impedance increase happened.

The first charge of identical cell with uncoated NMC is shown in Fig. 8a. HFR was 41 Ω . Characteristic impedances were much larger than the cell with NMC-LLSTO. The initial Nyquist plot showed an impedance of 1794 Ω , 3.1 \times higher than the cell with coating. The trend during charge was however similar, as impedance reached a minimum from 3.52 V to 3.67 V of about 1110 Ω . This was 5 \times higher than the minimum in the coated cell. At the end of charge the impedance increased again to 1590 Ω , 5.4 \times higher than the coated cell.

The uncoated cell reached a lower open circuit voltage than the coated cell, only 3.77 V compared to 3.92 V, although they both had a

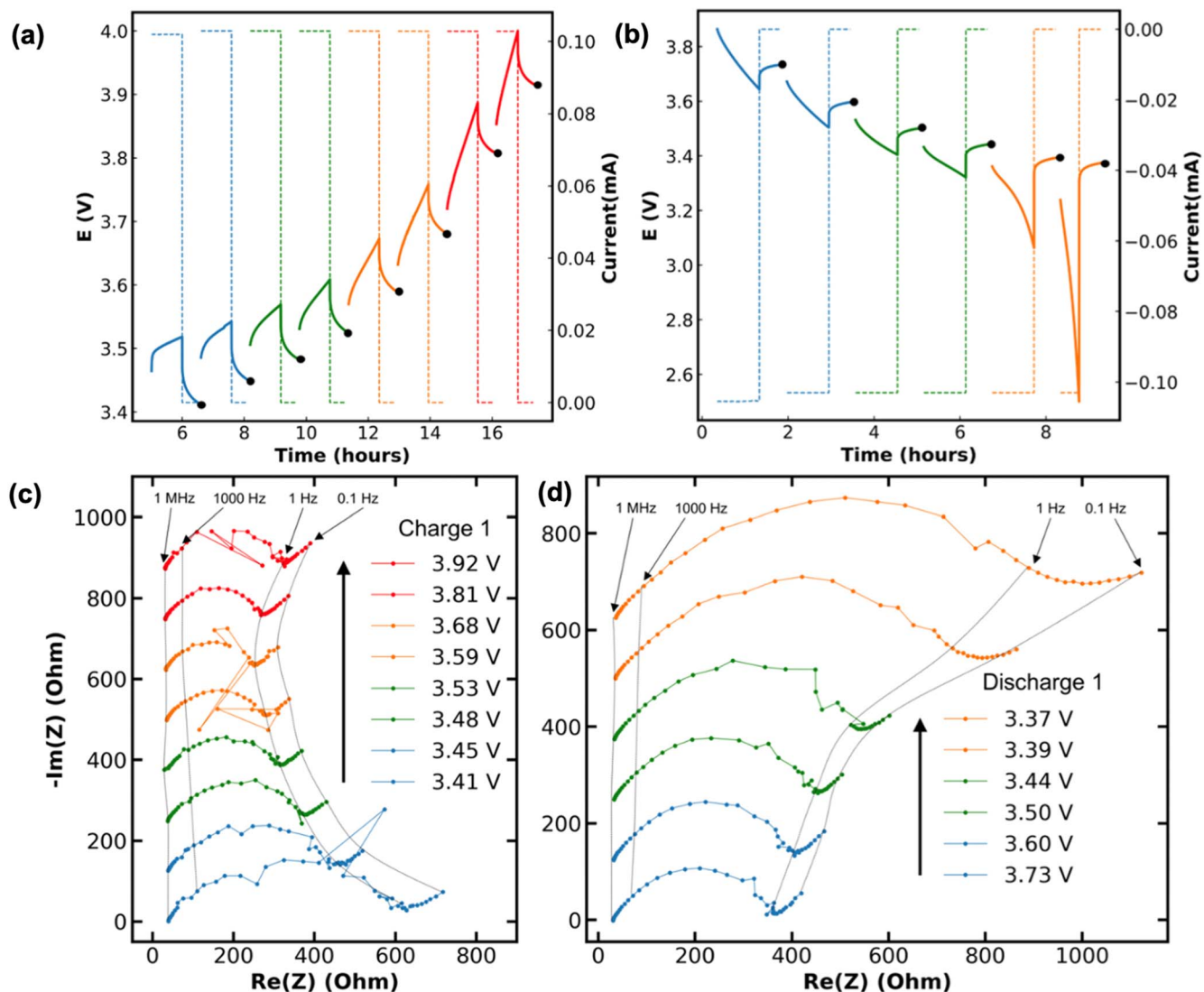


Figure 7. Piecewise in situ EIS during the first charge and discharge of a full cell with coated NMC-LLSTO, (Li/In₁Li₆PS₅Cl₁ NMC111-LLSTO/Li₆PS₅Cl). (a) Electrochemical data during charge, with EIS points marked in black. (b) Electrochemical data during discharge. (c) Nyquist plots corresponding to the charge steps and (d) Nyquist plots corresponding to the discharge steps.

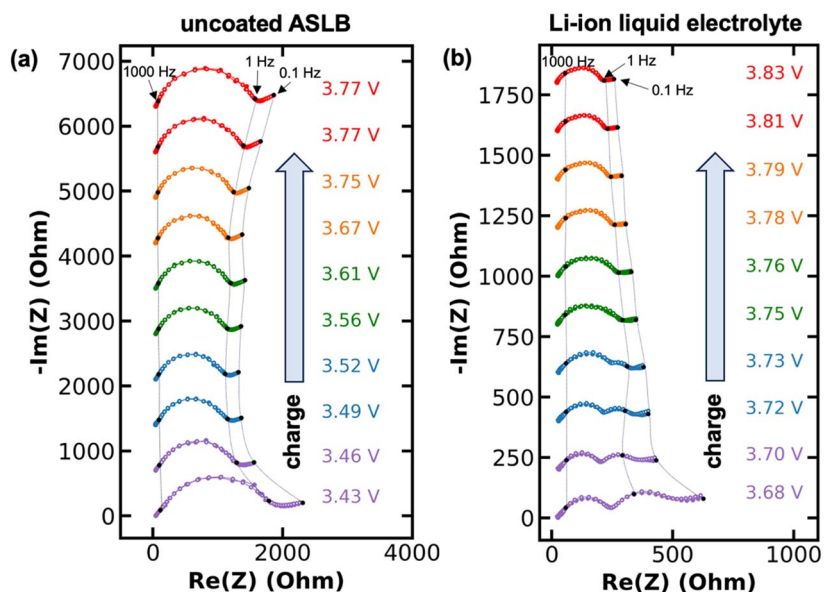


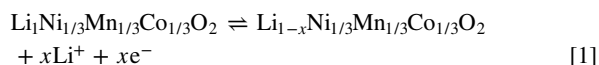
Figure 8. Piecewise in situ EIS performed during the first charge presented as Nyquist plots. The corresponding cell voltages are shown in the same color as the EIS data. (a) The uncoated ASLB full cell, (Li/In₁Li₆PS₅Cl₁ NMC111/Li₆PS₅Cl). Model fitting is shown with open circles. (b) A traditional Li-ion cell with liquid electrolyte of similar areal loading (5.6 mg cm⁻²).

4 V cutoff. This was because the higher overall impedance caused a larger iR contribution, therefore triggering the cutoff voltage earlier. While the overall trend was the same, the increasing impedance disparity with the coated cell ($3.1\times$ to $5\times$ to $5.4\times$) revealed that the decomposition reactions triggered by the electrochemical reaction caused a greater impedance rise in the uncoated cell.

Figure 8b shows the same experiment with a Li-ion cell of similar loading with liquid electrolyte. The first Li-ion Nyquist plot had two semicircles. The semicircle at higher frequency is typically attributed to Li^+ migration through the SEI, and the one at lower frequency is the charge transfer resistance of the NMC electrochemical reaction. By 3.75 V these two distinct processes had merged into a single semicircle. The characteristic impedance decreased steadily during charge. At 3.75 V it was 267 Ω and at the end of charge it was 202 Ω . These were lower than the coated ASLB cell, but only by a relatively small amount.

This impedance analysis demonstrated the difference between chemical and electrochemical degradation at the LPSC-NMC interface. The chemical degradation resulted in an interphase characterized by μXANES , and this interphase caused the uncoated cell to have a far higher initial impedance than the corresponding coated cell. While the impedances seen during charge of the coated ASLB did not differ greatly from a liquid electrolyte cell, the uncoated cell displayed much higher impedance. Electrochemical degradation was evident in the coated cell, which developed high impedance during the discharge, not returning to its pre-charged state. The coated and uncoated cells displayed the same trend during the initial charge, but the impedance of the uncoated cell increased to a greater extent. This suggested that coating also mitigates electrochemical decomposition.

Transmission line model of the cell with uncoated NMC.—The electrochemically active surface area in ASLBs is likely lower than in liquid electrolyte batteries because solid electrolyte does not flow and wet interfaces like liquid electrolyte. Instead, point contacts between the solid electrolyte and active material particles are the locations of electrochemical activity.^{17,30} Evidence of an interphase region containing reduced Co^{2+} was observed above. From the EIS, a high initial impedance was observed for uncoated ASLBs. This interphase layer presumably also can occlude the electrochemically active surface area. This is where the electrochemical reaction can occur, given in Eq. 1.



Microstructural information about a composite cathode can in principle be extracted from EIS data, but this requires application of a model. It is desired that the model should be physically meaningful and have few enough parameters that can reasonably be obtained by data fitting.

Single-particle or single-interface models can apply when current is uniform through the thickness of the composite cathode, i.e. when all surface area experiences the same extent of reaction. We have previously reported spatially-resolved non-uniformity in the electrochemical reaction during ASLB cycling in 120 μm thick cathodes.¹⁷ In such a thick cathode with 70% CAM, the maximum gradient in $1-x$ was measured to be 29% of the total cyclable cathode capacity.

Figure 9 shows *operando* EDXRD data on a thinner, 10 μm cathode, the same size as used in the EIS work above. Charge and discharge in Fig. 9a were correlated to the localized NMC a and c lattice parameters in Fig. 9b. These are reported as a function of depth in the cathode, with the distance from the LPSC separator represented by different colors. Using literature data for NMC111, the localized values of $1-x$ were calculated and are shown in Fig. 9c.³¹ As expected, non-uniformity was far less than in thicker cathodes. However, during the maximum non-uniformity, around 3.5 h or the midpoint of charge 1, the gradient in $1-x$ was 0.05 or 10% of the cyclable capacity.

The decomposed interphase around NMC particles could not be observed by EDXRD. Because the sampled gauge volume contained many particles, any signal from the interphase region was extremely small, being dominated by the bulk signal. We previously demonstrated structural decomposition of a sulfide solid electrolyte using EDXRD.³² This large-scale decomposition occurred when carbon was present in the cathode. However, with carbon excluded it was not observed.

A TLM is represented by a ladder-like circuit such as Fig. 10a, in which there are two parallel rails: one for ionic conduction and one for electronic conduction.³³ The electrochemical reaction in Eq. [1] demonstrates that both ionic (Li^+) and electronic (e^-) conduction are required for any particular reaction site on the NMC to participate in cycling. In Fig. 10a, one example reaction site is marked by a red dot. During charge, Li^+ and e^- transport away from this deintercalation site, as shown by dashed lines. These transport processes accomplish current flow across the composite cathode and complete the cell circuit. In this way the two rails of the TLM are connected by an interfacial impedance Z_{int} (Fig. 10b). The parallel RC circuit in Z_{int} accounts for the electrochemical reaction kinetics (R_1) and the interfacial capacitance (C_1) and has an impedance of $Z_{\text{RC}} = R_1/(1+j\omega C_1 R_1)$, where j is the imaginary number and ω is frequency. Solid-state diffusion of Li^+ in the NMC crystallites is represented by a constant phase element (CPE), with $Z_{\text{CPE}} = Q_2/(j\omega)^{a_2}$. For semi-infinite planar diffusion a Warburg element would be used with $a_2 = 0.5$, but in this system the more general CPE allowed for deviations from ideal geometry. This is a modification of the Randles circuit used to describe electrochemical reactions.^{34,35} Figure 10c shows the electronic end element Z_q , accounting for the contact resistance between the cathode and the metal current collector. Use of a CPE here allowed the model to also account for any capacitive behavior at the current collector. However, the fit results showed a_q was nearly zero, making this almost a pure resistor (see below).

In a TLM, there are an integral number of possible reaction sites, shown as n Z_{int} elements. This accounts for the fact that the electrochemical reaction does not have to occur uniformly throughout the electrode but can be preferentially distributed through the thickness. This phenomenon is often seen in composite electrodes, due to the coupling of transport and kinetics shown in Fig. 10a.³⁶ An early example of a TLM was provided by De Levie in 1967.³⁷ In the De Levie model, current enters and exits the circuit on different rails, as in the cathode model shown in Fig. 10a. Later, Siroma et al. provided several equations for general TLMs, one of which is the De Levie model.³⁸ In cases where the reaction is uniform, a single-interface equivalent circuit model can adequately model the system, and this has frequently been used in the study of ASLBs.^{5,39-41} However, in our system the EDXRD results above demonstrated that the reaction was non-uniform, requiring a TLM approach.

Equivalent circuit EIS models are meant to characterize multiple phenomena that occur on different time scales. This was important for our system, which we previously found to be transport-limited, making kinetics difficult to characterize using EDXRD data alone.¹⁷ However, they are usually more simplistic than physics-based models, sacrificing some accuracy for ease of interpretation. For example, current flow in liquid electrolyte is not solely a conduction phenomenon. Geng et al. have combined a TLM framework with physically-meaningful descriptions of transport and species concentration.⁴² Moškon et al. have developed powerful TLM versions that can account for realistic transference numbers in the liquid electrolyte of Li-ion batteries.^{43,44} However, ASLBs based on single-ion conductors like sulfides are particularly well-suited for analysis with a TLM, because ionic current is solely carried by Li^+ . In this way, an ASLB can be more accurately modeled with a TLM than a liquid electrolyte cell. Recently TLMs have been reported in analysis of ASLBs, to quantify both conduction and kinetic phenomena.^{10,13,45}

TLMs can be used to quantify details about electrode microstructure. Costard and co-workers used a TLM to determine the

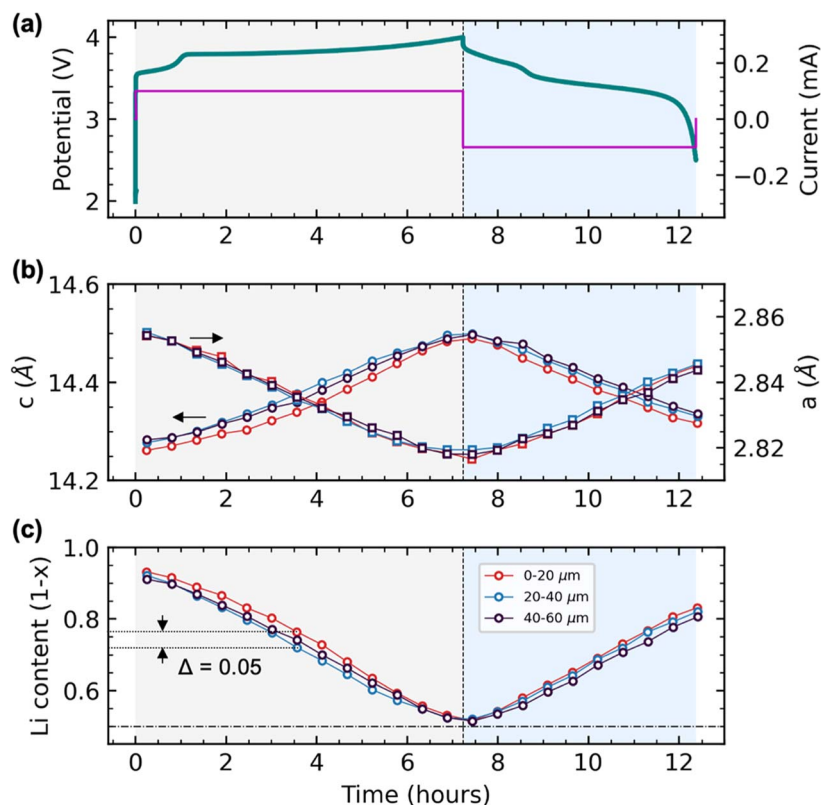


Figure 9. Operando EDXRD of the initial charge and discharge of a composite cathode with coated NMC. (a) Cycling data. (b) NMC111 lattice parameters a and c refined from the operando diffraction. (c) Li content $1-x$ as a function of depth in the cathode. Legend shows distance from the separator. At 3.5 h the maximum gradient in $1-x$ was 0.05, or 10% of the theoretical capacity.

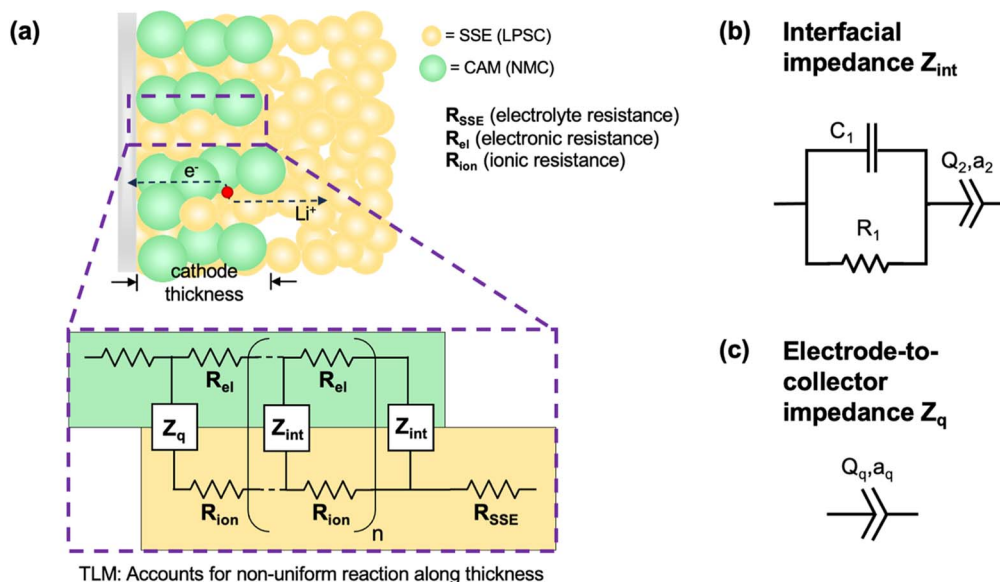


Figure 10. Equivalent circuit model used to analyze EIS results. (a) Transmission line model (TLM), which accounts for non-uniform reaction along the thickness of a composite cathode. (b) The Randles-type circuit used for the interfacial impedance Z_{int} . (c) The electrode-to-collector impedance Z_q .

kinetic parameters for charge transfer between NMC active material and liquid electrolyte.⁴⁶ For several NMC stoichiometries, they calculated values of the charge transfer resistance that were independent of the electrode microstructure, normalized to the real electrochemically active surface area A_{act} between NMC particles and the electrolyte.⁴⁷ This allowed calculation of true exchange current density i_0 values. Their approach was to determine A_{act} independently via FIB-SEM tomography. The charge transfer resistance R_{CT} obtained from fitting EIS data to a TLM could then be normalized with this true surface area. The four electrodes they studied had quite different microstructural properties, but their calculated i_0 parameters fell in a compact range from

2.08–4 A/m². This is as opposed to the rather large range of i_0 parameters reported across the literature from various methods.

Our approach in this work was to adapt the TLM technique reported by Costard et al., but to determine the real active surface area A_{act} . To do this, we assumed the microstructure-independent i_0 matches the average values found from literature. By determining R_{CT} via a TLM, A_{act} could thus be calculated. This approach addresses the difficulty of accurately determining the microstructural parameters, e.g. A_{act} , for the ASLBs used in this study. Sulfide ASLBs are typically studied under heavy compression, and it has been shown that performance is a function of the stack pressure.^{48,49} In the composite cathode, high cycling pressure is likely to increase

A_{act} , pressing sulfide particles into more intimate contact with the active material. Contact area between the sulfide particles themselves and between active material particles will also increase the cross sections of conduction pathways, improving effective conductivities. Tomographic FIB-SEM would be challenging to accomplish under compression. Nanoprobe X-ray tomography has demonstrated that contact area improves under compression.⁴⁹ However, if the area is blocked by an interphase formed through decomposition, this may be mere nm in thickness and difficult to observe via tomography. We hypothesize that an estimate of A_{act} can however be extracted from EIS through the application of a TLM in this work.

Impedance of the composite cathode TLM in Fig. 10a Z_{CC} was mathematically given by Eq. 2.

$$Z_{CC}(\omega) = \frac{R_{ion}R_{el}L}{R_{ion} + R_{el}} + \frac{\sqrt{Z_{int}}}{(R_{ion} + R_{el})^{\frac{3}{2}}} \cdot \frac{(R_{ion}^2 + R_{el}^2) \cosh\left(L\sqrt{\frac{R_{ion} + R_{el}}{Z_{int}}}\right) + 2R_{ion}R_{el} + \frac{1}{Z_q} \cdot R_{ion}^2 \sqrt{Z_{int}(R_{ion} + R_{el})} \sinh\left(L\sqrt{\frac{R_{ion} + R_{el}}{Z_{int}}}\right)}{\sinh\left(L\sqrt{\frac{R_{ion} + R_{el}}{Z_{int}}}\right) \frac{1}{Z_q} \sqrt{Z_{int}(R_{ion} + R_{el})} \cosh\left(L\sqrt{\frac{R_{ion} + R_{el}}{Z_{int}}}\right)} \quad [2]$$

This is the Z-type open-Q arrangement as defined by Siroma et al.³⁸ This impedance was placed in series with a resistance for the solid-state separator layer, R_{SSE} , as well as an RQ circuit that modeled the In-Li anode foil. The values for the separator and anode parameters were determined from symmetric cell experiments and were held constant during EIS data fitting for the full cells. Fitting was done for the data in Fig. 8a, using a non-linear least squares regression in Python.

Before using the TLM fits to quantify the microstructure and calculate A_{act} , we first normalized to an electrode length scale, to allow comparison to literature results normalized in a similar way. This confirmed the fitted values were reasonable. The raw fit parameters were normalized using the cell superficial area 1.247 cm² and are reported in Table I. The fits for the seventh EIS step (112 mAh g⁻¹) showed relatively anomalous values that disagreed with the trends in the rest of the charge. This indicated fitting of this step was prone to error, although it is included in Table I for completeness.

Charge transfer resistance r_{CT} was equal to r_1 from the interfacial impedance. The trend in charge transfer resistance r_{CT} described changes in the electrochemical reaction during battery charging. In liquid electrolyte cathodes, r_{CT} is reported to initially decrease during the charge.⁵⁰ In contrast, the ASLB r_{CT} started at 25 Ω cm² (at 16 mAh g⁻¹) and increased to 117 Ω cm² (32 mAh/g) and 169 Ω cm² (48 mAh g⁻¹). Beginning at 64 mAh g⁻¹ it decreased to 112 mAh g⁻¹. In the final charge step, there was another increase, to a final value of 98.9 Ω cm².

To assess the validity of the model fits, these values were compared to reported r_{CT} values from the literature. Charbonneau, et al. measured r_{CT} for NMC111 in liquid electrolyte.⁵⁰ They found r_{CT} decreased until 100 mAh g⁻¹ with minimum values of 1.92 Ω cm². Moškon, et al. used EIS and a TLM to model NMC811-

Li cells using varying concentrations of LiPF₆ liquid electrolyte.⁴³ They reported values for a 1M electrolyte adjusted for their electrode area (2 cm²) giving an r_{CT} of 32 Ω cm² for pristine NMC811. Costard, et al. used EIS, TLM, and Butler-Volmer kinetics to calculate parameters for NMC111, NMC622, and blended cathodes.⁴⁶ They found r_{CT} of 63.97 Ω cm².

While there is a significant variation in r_{CT} values reported in the literature, the values in our study were within reasonable ranges. This provided confidence that the model delivered physically meaningful results. Double layer capacitance c_{dl} was equal to c_1 . We also compared c_{dl} to literature values, which are generally in the mF/cm² to μ F/cm² range. Moškon, et al. found a c_{dl} of 5 mF cm⁻² for pristine NMC811.⁴³ Charbonneau, et al. measured a value of 1.1 mF cm⁻².

Calculation of electrochemically active surface area A_{act} .—In this section we used the raw fit parameters to calculate A_{act} , using a method similar to that in Costard et al., detailed above. In the literature, values from equivalent circuit models are often normalized by the electrode superficial area. The values in Table I were normalized this way, to compare directly with literature values. However, a more physically meaningful normalization can be done using the electrochemically active surface area in the cathode, A_{act} . For example, R_{CT} can be converted to an area normalized r_{CT} using Eq. 3.⁴⁶

$$r_{CT} = R_{CT} \cdot A_{act} \quad [3]$$

This provides a way to estimate A_{act} from EIS data. Because solid electrolyte does not flow to wet the active material in the manner of liquid electrolyte, it is believed that A_{act} will be lower than in conventional liquid electrolyte cells. This can be due to voids in the composite cathode causing reduced contact between SSE and NMC. Other phenomena will also result in reduction of A_{act} , for example growth of a resistive interphase or physical disconnection of the NMC caused by volume change.⁵

Active surface area is often reported as volume specific active surface area a_{act} , given by Eq. 4.

$$a_{act} = \frac{A_{act}}{\text{Volume of electrode}} \quad [4]$$

A theoretical calculation for a_{act} in a porous electrode can be derived based on the active material diameter and the volume fractions of the active material and electrolyte phases.⁵¹ Based on a 10 μ m NMC particle diameter and the densities of NMC and LPSC, a theoretical a_{act} value of 2216 cm⁻¹ is expected for the ASLB system. In the section that follows, we use an alternative calculation based on R_{CT} to estimate the real active surface area in the ASLB.

The Butler-Volmer equation describes charge transfer kinetics at the interface between cathode active material and SSE and is displayed in Eq. 5. Here n is the number of electrons transferred, i_0 is the exchange current density, η is the surface overpotential, and α is typically 0.5. Based on a literature review in Table II of

Table I. Superficial area-normalized parameters from TLM data fitting of the uncoated ASLB EIS results.

Charged capacity mAh/g	r_1 [Ω cm ²]	c_1 [mF/cm ²]	$\frac{q_2}{2^2 - a^2}$ [Ω cm ² s ^{-a2}]	a_2	$\frac{q_q}{s^{-ap}}$ [Ω cm ² s ^{-ap}]	a_q
16	25.2	0.363	0.028	0.016	44500	0.053
32	117	0.050	5.13	0.197	84700	0.034
48	169	0.030	16.8	0.216	118000	0.024
64	104	0.045	9.83	0.214	136000	0.024
80	86.7	0.053	9.73	0.221	151700	0.021
96	66.4	0.071	7.82	0.235	154300	0.018
112	28.1	0.161	4.31	0.240	192800	0.012
128	98.9	0.046	15.4	0.255	194700	0.009

Table II. Literature review of i_0 values reported for NMC111.

i_0 [A/cm ²]	Electrolyte	References
4.0×10^{-4}	1 M LiPF ₆ in EC/DMC (1:1)	46
1.3×10^{-4}	1 M LiPF ₆ in EC:DMC:EMC (1:1:1)	52
5.0×10^{-4}	1 M LiPF ₆ in EC:DMC:EMC (1:1:1)	53
8.2×10^{-5}	Unknown commercial electrolyte	53
1.5×10^{-4}	From model	54
8.0×10^{-4}	1 M LiPF ₆ in 1:1 EC/DEC	55
3.0×10^{-6}	1 M LiPF ₆ in EC/DMC (1:1)	56
3.8×10^{-6}	1 M LiPF ₆ in DMC	57
5.4×10^{-5}	Unknown commercial electrolyte	58
1.4×10^{-4}	1 M LiPF ₆ in EC:EMC:DMC (1:1:1 v/v)	59

Table III. Calculated values of electrochemically active surface area (A_{act}) and volume specific active surface area (a_{act}).

Charged capacity mAh/g	A_{act} [cm ²]	a_{act} [cm ² /cm ³]
16	5.43	1090
32	1.17	234
48	0.81	162
64	1.31	262
80	1.58	316
96	2.06	413
112	4.87	975
128	1.38	277

exchange current density of NMC111, an average i_0 value of 2.3×10^{-4} A cm⁻² was used.⁴⁶

$$i_{CT} = i_0 \left[\exp\left((1 - \alpha) \frac{nF\eta}{RT} \right) - \exp\left((-\alpha) \frac{nF\eta}{RT} \right) \right] \quad [5]$$

For small currents like those applied during EIS, a linear approximation of the BV equation can be used, as in Eq. 6.

$$i_{CT} = i_0 \frac{nF\eta}{RT} \quad [6]$$

The area specific charge transfer resistance r_{CT} is equal to overpotential divided by charge transfer current as seen in Eq. 7.

$$r_{CT} = \frac{\eta}{i_{CT}} = \frac{RT}{i_0 F} = R_{CT} A_{act} \quad [7]$$

Equation 7 can therefore be used to solve for the active surface area in the system A_{act} given known values for R_{CT} and i_0 . This is given in Eq. 8.

$$A_{act} = \frac{RT}{i_0 F (R_{CT})} \quad [8]$$

Table III displays the calculated values of A_{act} and a_{act} based on the non-normalized values of R_{CT} obtained from the EIS fitting.

A theoretical a_{act} value of 2216 cm⁻¹ was calculated for the ASLB system. The values of a_{act} in Table III were all lower than this value, indicating the inefficient packing of solid particles in an ASLB results in lower active surface area. Interphase formation and disconnection due to volume change are also expected to impact this value. Early in the charge (16 mAh g⁻¹) the a_{act} value was calculated to be 49% of the theoretical value. The tomography data of Sakka et al. showed that with similar materials and the same compression (50 MPa) the contact area fraction between NMC and sulfide was 84%.⁴⁹ The lower value estimated from the TLM could be due to the decomposition interphase

blocking the connection even in cases where particles are touching. Because the tomography voxel was 500 nm, the interphase and small disconnections might not be discernible. This demonstrates that chemical decomposition results in reduced charge transfer between the active material and electrolyte.

The sudden drop in a_{act} to 234 cm⁻¹ following the first segment is the most prominent observation upon continued charging. Because of uncertainty inherent in the EIS fitting and the selection of i_0 , the variation after segment 2 is possibly due to experimental variations. To compare active surface area more generally, we use the median value of 296 cm⁻¹. This is 7.5× lower than the theoretical value of 2216 cm⁻¹, or 13%. This is far lower than the 84% value calculated by tomography. Due to the voxel size, tomography may only be able to observe loss of contact area when it is caused by pore space. The extra loss could be due to physical disconnection or additional electrochemical interphase formation. Our finding demonstrates that contact areas may be lower than expected in ASLBs, especially when using uncoated active material that undergoes decomposition and interphase formation.

The use of a TLM and piecewise EIS has been shown as a possible tool to probe microstructural characteristics of composite ASLB electrodes, especially in cases where active surface may be blocked by extremely small interphase layers that are difficult to observe in situ. Future efforts to produce composite electrodes with well-controlled microstructures could be used to tie microstructure characteristics to TLM parameters, which can be useful for more extensive cell characterization.

Conclusions

The Li₆PS₅Cl-NMC111 interface without a coating was studied by μ XANES and through EIS analysis. A chemically-formed interphase was detected by μ XANES, evident from reduction of Co at an uncoated NMC particle surface. This interphase was produced by decomposition at rest, and for this reason it was chemical in nature. The effect of this interphase was observed in piecewise EIS data, where a large impedance was observed in an ASLB fabricated with uncoated NMC. In contrast, a cell with coated NMC-LLSTO showed smaller impedances. The Co-containing layer presumably occluded the electrochemically active area, which is the area of contact between the LPSC electrolyte particles and the NMC particles. This is where the electrochemically active interface is, and where the electrochemical reaction can occur. By using a TLM to fit piecewise EIS data, characteristic parameters of the system were determined. The charge transfer resistance R_{CT} was used to estimate the volume specific active surface area (a_{act}). The median value for a_{act} was 296 cm⁻¹, a factor of 7.5 lower than the theoretical value of 2216 cm⁻¹ or 13%. This provided evidence of a lower electrochemically active surface area in the ASLB. The decomposition and passivation at this unstabilized solid-solid interface were shown to potentially throttle performance through both active material loss and impedance growth, reducing active surface area. Therefore strategies to stabilize this interface are critical to realizing the high stability of sulfide electrolytes based ASLBs.

Acknowledgments

A.M.S., X.S., H.Z., and J.W.G. acknowledge financial support from the National Science Foundation under Award Number CBET-ES-1924534. K.C.W. acknowledges support from the Northeastern University Office of Undergraduate Research and Fellowships via a PEAK Summit Award. This research used the 5-ID (SRX) beamline of the National Synchrotron Light Source II, a U.S. Department of Energy (DOE) Office of Science User Facility operated for the DOE Office of Science by Brookhaven National Laboratory under Contract No. DE-SC0012704. This research used resources of the Advanced Photon Source beamline 6-BM, a U.S. Department of Energy (DOE) Office of Science User Facility operated for the DOE Office of Science by Argonne National Laboratory under Contract

No. DE-AC02-06CH11357. The authors would also like to acknowledge Robert Egan from Northeastern Universities ChemE Machine Shop for his assistance in designing and building the in situ cell and stage mounts.

ORCID

Joshua W. Galloway  <https://orcid.org/0000-0002-6798-7781>

References

- M. B. Dixit, J.-S. Park, P. Kenesei, J. Almer, and K. B. Hatzell, *Energy Environ. Sci.*, **14**, 4672 (2021).
- A. L. Davis, V. Goel, D. W. Liao, M. N. Main, E. Kazyak, J. Lee, K. Thornton, and N. P. Dasgupta, *ACS Energy Lett.*, **6**, 2993 (2021).
- J.-M. Doux, Y. Yang, D. H. Tan, H. Nguyen, E. A. Wu, X. Wang, A. Banerjee, and Y. S. Meng, *J. Mater. Chem. A*, **8**, 5049 (2020).
- J. A. Lewis, C. Lee, Y. Liu, S. Y. Han, D. Prakash, E. J. Klein, H.-W. Lee, and M. T. McDowell, *ACS Appl. Mater. Interfaces*, **14**, 4051 (2022).
- R. Koerver, I. Aygün, T. Leichtweiß, C. Dietrich, W. Zhang, J. O. Binder, P. Hartmann, W. G. Zeier, and J. Janek, *Chem. Mater.*, **29**, 5574 (2017).
- D. Cao, Y. Zhang, A. M. Nolan, X. Sun, C. Liu, J. Sheng, Y. Mo, Y. Wang, and H. Zhu, *Nano Lett.*, **20**, 1483 (2020).
- Q. Zhang, A. M. Bruck, A. M. Stavola, W. Liang, P. Aurora, and J. W. Galloway, *Batteries & Supercaps*, **4**, 529 (2020).
- H. Komatsu, S. Banerjee, M. L. Holekevi Chandrappa, J. Qi, B. Radhakrishnan, S. Kuwata, K. Sakamoto, and S. P. Ong, *J. Phys. Chem. C*, **126**, 17482 (2022).
- J. Auvergniot, A. Cassel, J.-B. Ledeuil, V. Viallet, V. Seznec, and R. Dedryvère, *Chem. Mater.*, **29**, 3883 (2017).
- S.-K. Jung, H. Gwon, S.-S. Lee, H. Kim, J. C. Lee, J. G. Chung, S. Y. Park, Y. Aihara, and D. Im, *J. Mater. Chem. A*, **7**, 22967 (2019).
- Y. Zhu, X. He, and Y. Mo, *ACS Appl. Mater. Interfaces*, **7**, 23685 (2015).
- I. A. J. Gordon, S. Grugeon, H. Takenouti, B. Tribollet, M. Armand, C. Davoisne, A. Débart, and S. Laruelle, *Electrochim. Acta*, **223**, 63 (2017).
- P. Minnmann, L. Quillman, S. Burkhardt, F. H. Richter, and J. Janek, *J. Electrochem. Soc.*, **168**, 040537 (2021).
- J. Zhang, C. Zheng, L. Li, Y. Xia, H. Huang, Y. Gan, C. Liang, X. He, X. Tao, and W. Zhang, *Adv. Energy Mater.*, **10**, 1903311 (2019).
- W. Zhang et al., *ACS Appl. Mater. Interfaces*, **9**, 17835 (2017).
- M. B. Dixit, M. Regala, F. Shen, X. Xiao, and K. B. Hatzell, *ACS Appl. Mater. Interfaces*, **11**, 2022 (2018).
- A. M. Stavola, X. Sun, D. P. Guida, A. M. Bruck, D. Cao, J. S. Okasinski, A. C. Chuang, H. Zhu, and J. W. Galloway, *ACS Energy Lett.*, **8**, 1273 (2023).
- B.-Y. Tsai, S.-K. Jiang, Y.-T. Wu, J.-S. Yang, S.-H. Wu, P.-C. Tsai, W.-N. Su, C.-Y. Chiang, and B. J. Hwang, *J. Phys. Chem. C*, **127**, 14336 (2023).
- D. Cao, Y. Zhang, A. M. Nolan, X. Sun, C. Liu, J. Sheng, Y. Mo, Y. Wang, and H. Zhu, *Nano Lett.*, **20**, 1483 (2019).
- E. Nazaretski, D. Coburn, W. Xu, J. Ma, H. Xu, R. Smith, X. Huang, Y. Yang, L. Huang, and M. Idir, *J. Synchrotron Radiat.*, **29**, 1284 (2022).
- L. Li, H. Yan, W. Xu, D. Yu, A. Heroux, W.-K. Lee, S. Campbell, and Y. Chu, *PyXRF: Python-based X-ray fluorescence analysis package*, ed. B. Lai and A. Somogyi (SPIE, San Diego, California, United States) X-Ray Nanoimaging: Instruments and Methods III, Proceedings Volume 10389 (2017).
- B. Ravel and M. Newville, *J. Synchrotron Radiat.*, **12**, 537 (2005).
- B. G. Hudson and S. E. Mason, *Applied sciences*, **12**, 4065 (2022).
- R. Qiao, J. Liu, K. Kourtakis, M. G. Roelofs, D. L. Peterson, J. P. Duff, D. T. Deibler, L. A. Wray, and W. Yang, *J. Power Sources*, **360**, 294 (2017).
- J. L. White, F. S. Gittleson, M. Homer, and F. El Gabaly, *J. Phys. Chem. C*, **124**, 16508 (2020).
- H. Shin, M. Kim, N. Kim, C. Jung, J. Chung, K. Kim, and W. S. Jeon, *J. Phys. Chem. Solids*, **148**, 109732 (2021).
- C. H. van Oversteeg, H. Q. Doan, F. M. de Groot, and T. Cuk, *Chem. Soc. Rev.*, **46**, 102 (2017).
- M. Risch, V. Khare, I. Zaharieva, L. Gerencser, P. Chernev, and H. Dau, *J. Am. Chem. Soc.*, **131**, 6936 (2009).
- P. Luo, H. Zhang, L. Liu, Y. Zhang, J. Deng, C. Xu, N. Hu, and Y. Wang, *ACS Appl. Mater. Interfaces*, **9**, 2500 (2017).
- A. Bielefeld, D. A. Weber, and J. R. Janek, *ACS Appl. Mater. Interfaces*, **12**, 12821 (2020).
- I. Buchberger, S. Seidlmayer, A. Pokharel, M. Piana, J. Hattendorff, P. Kudejova, R. Gilles, and H. A. Gasteiger, *J. Electrochem. Soc.*, **162**, A2737 (2015).
- X. Sun, A. M. Stavola, D. Cao, A. M. Bruck, Y. Wang, Y. Zhang, P. Luan, J. W. Galloway, and H. Zhu, *Adv. Energy Mater.*, **11**, 2002861 (2021).
- M. E. Orazem and B. Tribollet, "Electrochemical impedance spectroscopy." *New Jersey*, **1**, 383 (2008).
- E. Katz, "Electrochemical contributions: John Edward Brough Randles (1912–1998)." *Electrochem. Sci. Adv.*, **3**, e2300005 (2023).
- J. E. B. Randles, *Discuss. Faraday Soc.*, **1**, 11 (1947).
- J. S. Newman and C. W. Tobias, *J. Electrochem. Soc.*, **109**, 1183 (1962).
- D. Levie, *Adv. Electrochem. and Electrochem. Eng.*, **6**, 329 (1967).
- Z. Siroma, N. Fujiwara, S.-I. Yamazaki, M. Asahi, T. Nagai, and T. Ioroi, *Electrochim. Acta*, **160**, 313 (2015).
- P. Hu, Y. Zhang, X. Chi, K. Kumar Rao, F. Hao, H. Dong, F. Guo, Y. Ren, L. C. Grabow, and Y. Yao, *ACS Appl. Mater. Interfaces*, **11**, 9672 (2019).
- W. Zhang, F. H. Richter, S. P. Culver, T. Leichtweiss, J. G. Lozano, C. Dietrich, P. G. Bruce, W. G. Zeier, and J. R. Janek, *ACS Appl. Mater. Interfaces*, **10**, 22226 (2018).
- T. Shi, Y.-Q. Zhang, Q. Tu, Y. Wang, M. Scott, and G. Ceder, *J. Mater. Chem. A*, **8**, 17399 (2020).
- Z. Geng, S. Wang, M. J. Lacey, D. Brandell, and T. Thiringer, *Electrochim. Acta*, **372**, 137829 (2021).
- J. Moškon, J. Žuntar, S. Drvarič Talian, R. Dominko, and M. Gaberšček, *J. Electrochem. Soc.*, **167**, 140539 (2020).
- J. Moškon and M. Gaberšček, *Journal of Power Sources Advances*, **7**, 100047 (2021).
- S. Ohno, C. Rosenbach, G. F. Dewald, J. Janek, and W. G. Zeier, *Adv. Funct. Mater.*, **31**, 2010620 (2021).
- J. Costard, J. Joos, A. Schmidt, and E. Ivers-Tiffée, *Energy Technology*, **9**, 2000866 (2021).
- A. Banerjee, X. Wang, C. Fang, E. A. Wu, and Y. S. Meng, *Chemical Reviews*, **120**, 6878 (2020).
- Y.-T. Chen, J. Jang, J. A. S. Oh, S.-Y. Ham, H. Yang, D.-J. Lee, M. Vicencio, J. B. Lee, D. H. Tan, and M. Chouchane, *Enabling Uniform and Accurate Control of Cycling Pressure for All-Solid-State Batteries*, **ChemRxiv** (2023).
- Y. Sakka, H. Yamashige, A. Watanabe, A. Takeuchi, M. Uesugi, K. Uesugi, and Y. Orikasa, *J. Mater. Chem. A*, **10**, 16602 (2022).
- V. Charbonneau, A. Lasia, and G. Brisard, *J. Electroanal. Chem.*, **875**, 113944 (2020).
- T. F. Fuller and J. N. Harb, *Electrochemical Engineering* (Wiley, New York) (2018).
- J. Schmalstieg and D. U. Sauer, *J. Electrochem. Soc.*, **165**, A3811 (2018).
- J. Schmalstieg, C. Rahe, M. Ecker, and D. U. Sauer, *J. Electrochem. Soc.*, **165**, A3799 (2018).
- Y. Kerdja, M. Chandesris, and S. Martinet, *J. Power Sources*, **507**, 230250 (2021).
- M. Varini, J. Y. Ko, P. Svens, U. Mattinen, M. Klett, H. Ekström, and G. Lindbergh, *Journal of Energy Storage*, **31**, 101616 (2020).
- P.-C. Tsai, B. Wen, M. Wolfman, M.-J. Choe, M. S. Pan, L. Su, K. Thornton, J. Cabana, and Y.-M. Chiang, *Energy Environ. Sci.*, **11**, 860 (2018).
- B. Wen, Z. Deng, P.-C. Tsai, Z. W. Lebens-Higgins, L. F. J. Piper, S. P. Ong, and Y.-M. Chiang, *Nat. Energy*, **5**, 578 (2020).
- B. Csomós, D. Fodor, and I. Vajda, *Energies*, **13**, 6238 (2020).
- L. Wang, J. Zhao, X. He, J. Gao, J. Li, C. Wan, and C. Jiang, *Int. J. Electrochem. Sci.*, **7**, 345 (2012).